CrossMark

Fermi/GBM View of the 2019 and 2020 Burst Active Episodes of SGR J1935+2154

Lin Lin[1] , Ersin Göğüş[2] , Oliver J. Roberts[3] , Matthew G. Baring[4] , Chryssa Kouveliotou[5,6] , Yuki Kaneko[2] ,
Alexander J. van der Horst[5,6] , and George Younes[5,6]

[1] Department of Astronomy, Beijing Normal University, Beijing 100875, People's Republic of China; llin@bnu.edu.cn
[2] Sabancı University, Faculty of Engineering and Natural Sciences, İstanbul 34956, Turkey
[3] Science and Technology Institute, Universities Space and Research Association, 320 Sparkman Drive, Huntsville, AL 35805, USA
[4] Department of Physics and Astronomy—MS 108, Rice University, 6100 Main Street, Houston, TX 77251-1892, USA
[5] Department of Physics, The George Washington University, 725 21st Street NW, Washington, DC 20052, USA
[6] Astronomy, Physics, and Statistics Institute of Sciences (APSIS), The George Washington University, Washington, DC 20052, USA
Received 2020 August 11; revised 2020 October 2; accepted 2020 October 5; published 2020 October 21

Abstract

We present temporal and time-integrated spectral analyses of 148 bursts from the latest activation of SGR J1935 +2154, observed with the Fermi/Gamma-ray Burst Monitor from 2019 October 4 through 2020 May 20, excluding an ∼130 s segment with a very high burst density on 2020 April 27. The 148 bursts presented here are slightly longer and softer than bursts from earlier activations of SGR J1935+2154, as well as from other magnetars. The long-term spectral evolution trend is interpreted as being associated with an increase in the average plasma loading of the magnetosphere during bursts. We also find a trend of increased burst activity from SGR J1935+2154 since its discovery in 2014. Finally, we find no association of typical radio bursts with X-ray bursts from the source. This contrasts the association of FRB 200428 with an SGR J1935+2154 X-ray burst, which is to-date unique among the magnetar population.

Unified Astronomy Thesaurus concepts: Magnetars (992); Soft gamma-ray repeaters (1471)

Supporting material: machine-readable table

1. Introduction

Among the intriguing properties of extremely magnetized neutron stars (a.k.a magnetars; Duncan & Thompson 1992; Kouveliotou et al. 1998), repeated emission of very short, soft γ-ray bursts is probably their most characteristic attribute (for a review, see Kaspi & Beloborodov 2017). Burst emission has been detected, at different occurrence rates, from more than two-thirds of the magnetar population (Olausen & Kaspi 2014). The total energies of these typically short (∼0.1 s) events are very large, ranging anywhere from ∼10^{38} to 10^{42} erg, and very rarely ≳10^{44} erg during the several-minute-long Giant Flares (GFs; Hurley et al. 1999; Palmer et al. 2005).

SGR J1935+2154 was discovered when a short burst triggered the Burst Alert Telescope (BAT) on board the Neil Gehrels Swift Observatory (hereafter Swift) (Stamatikos et al. 2014). Pointed follow-up observations with the Swift/X-Ray Telescope, Chandra, and XMM-Newton revealed a spin period of 3.24 s and a period derivative of 1.43×10^{-11} s s^{-1}, and therefore an inferred equatorial surface magnetic field strength of 2.2×10^{14} G, thus establishing its magnetar nature (Israel et al. 2016). Subsequently, SGR J1935+2154 went into multiple short, burst-active episodes in 2015 and 2016, with tens of bursts during each episode (Younes et al. 2017; Lin et al. 2020a). From this perspective, SGR J1935+2154 is considered a prolific transient magnetar, according to the classifying scheme of Göğüş (2014).

In Lin et al. (2020a), we presented a comprehensive investigation of bursts from SGR J1935+2154 during its four active episodes in 2014, 2015, and 2016 (twice), detected with the Gamma-ray Burst Monitor (GBM) on board the Fermi Gamma-ray Space Telescope (Fermi) and Swift/BAT. During the detailed temporal and spectral analyses of these bursts, we found that the magnetar became more burst-active in every subsequent active episode, emitting 3, 24, 42, and 54 bursts in

2014, 2015, 2016 May, and 2016 June, respectively. The cumulative energy for each active episode was also observed to grow sequentially over the same time frame; ∼1×10^{39}, ∼4×10^{40}, ∼1×10^{41}, and ∼4×10^{41} erg, assuming a source distance of 9 kpc. Interestingly, we also found that the spectral behavior of these bursts evolved in time; bursts detected in 2016 were, on average, slightly harder than those in 2014 and 2015. This overall source evolution suggested that the next activation would likely be more intense.

SGR J1935+2154 was active again on 2019 October 4, when it emitted a solitary event. A month later, in 2019 November, the source entered a state of heightened activity; this is the first active episode reported in this paper. SGR J1935 +2154 returned back to a nonbursting state before resuming activity in late 2020 April. There was again, a solitary triggered event in the GBM data on April 10 and one additional event on April 22 detected with CALET, Konus-Wind, and IPN (Cherry et al. 2020; Hurley et al. 2020; Ridnaia et al. 2020a); GBM was Earth-occulted during the later burst.

On April 27, SGR J1935+2154 entered an extreme burst-active episode emitting hundreds of X-ray bursts over a few minutes (Palmer 2020; Younes et al. 2020b). Strikingly, a bright fast radio burst (FRB 200428) was detected on April 28 from the direction of SGR J1935+2154 (The CHIME/FRB Collaboration et al. 2020; Bochenek et al. 2020), contemporaneous with an X-ray burst from the source (Li et al. 2020a; Mereghetti et al. 2020; Ridnaia et al. 2020b). Younes et al. (2020a) demonstrated that this X-ray burst was spectrally different from all other bursts detected with GBM during the same active episode. Following FRB 200428, three weaker radio bursts from SGR J1935+2154 have been reported (Kirsten et al. 2020; Zhang et al. 2020). These were three to six magnitudes dimmer than FRB 200428, each without an

X-ray counterpart simultaneously detected (Kirsten et al. 2020; Li et al. 2020b).

In this study, we present detailed temporal and spectral analyses of 148 SGR J1935+2154 bursts detected with GBM during its 2019 (22 bursts) and 2020 (126 bursts) activities, excluding a period with a densely concentrated burst forest, whose analyses will be reported elsewhere (Y. Kaneko et al. 2020, in preparation). In the following section, we describe our deep search for untriggered bursts from SGR J1935 +2154 using the continuous high time resolution data of GBM, and elaborate on our data analysis methodology. We present our results in Section 3, and discuss their implications in Section 4.

2. Burst Search and Data Analysis

SGR J1935+2154 is visible for about half of the time by GBM owing to its wide unocculted field of view, which is afforded by 12 NaI detectors (8 keV−1 MeV) and two BGO scintillators (∼200 keV−∼30 MeV). A more detailed description of the instrument and scientific data types can be found in Meegan et al. (2009). Our analysis of magnetar bursts, which typically emit at energies <200 keV, is based on the continuous time-tagged event (CTTE) data of NaI detectors, which provide the highest temporal (2 μs) and spectral (128 channels) resolutions.

We analyzed the data for the 2019 and 2020 outbursts in a similar way to our previous studies of the same source (Lin et al. 2020a). A Bayesian Block algorithm (Scargle et al. 2013) was used to search for magnetar-like short bursts in the CTTE data. The algorithm splits up the data into blocks, with each block having a constant rate. This addresses the issue of characterizing any variability in the CTTE data by finding the optimal boundaries between each block, called change points. This allows us to separate statistically significant, valid events, from random noise using a nonparametric light curve analysis (Scargle et al. 2013). The false positive rate of a change point between two blocks was set to 5% for the entire search, using a prior number of change points through the data (Scargle et al. 2013). This iterative process is completed when all the parameters from the search are consistent. We searched for bursts in the intervals from 2019 September 25 through 2019 November 20 and 2020 April 1 through 2020 May 31. Besides SGR J1935+2154, SGR 1806−20 and Swift J1818.0-1607 were also occasionally active during our search intervals (Ambrosi et al. 2020; Barthelmy et al. 2020; Gronwall et al. 2020). All burst candidates found with our Bayesian Block search are localized using the Daughter Of Locburst code (von Kienlin et al. 2012). The average statistical uncertainty at 1σ confidence level of our sample is ∼4°.7, and the systematic uncertainty is ∼4°.4 (Lin et al. 2020a). The distance between SGR J1935+2154 and any of the other active magnetars is larger than the location uncertainties. We selected all bursts whose locations on the sky were consistent with SGR J1935 +2154. Table 1 lists each burst start time and temporal and spectral characteristics, while Table 2 gives a summary of the source activity during each episode.

During the onset of the outburst on April 27, SGR J1935 +2154 entered an energetic (fluence $F \sim 2.7 \times 10^{-4}$ erg cm^{-2} in the 8–200 keV band) period of activity, lasting ∼130 s. This burst forest was reported by several instruments; it is the first time such behavior has been observed from SGR J1935 +2154 since its discovery. During the forest, the bursts are superimposed on enhanced persistent emission. In this work, we exclude all bursts during this forest (from 18:31:30 to 18:33:40 UTC on 2020 April 27) to keep our sample consistent with that of our previous study (Lin et al. 2020a). For the bursts in our sample, we ascribe multiple peaks as belonging to the same burst if the time difference between their peaks is less than one-quarter of the spin period of SGR J1935+2154, following the convention of Göğüş et al. (2001). Our final burst sample comprises 148 bursts, of which 22 events were detected late 2019 and 126 early 2020 (see Table 1).

As in Lin et al. (2020a), we define an active bursting episode in this study as a period in which more than two bursts are emitted within 10 days of each other; bursts observed outside this period are excluded. Therefore, we identify two bursting episodes from SGR J1935+2154, which are shown in Figure 1. The properties of these episodes are summarized in Table 2. Note that the two isolated bursts (on 2019 October 4 and 2020 April 10) mentioned in Section 1 are included in Table 2 and the whole sample analysis, but are not part of the analyses of episodes 1 and 2.

3. Results

3.1. Temporal Analysis

The Bayesian block duration (τ_{bb}) is a product of our Bayesian burst search process. It is the total time length of all consecutive Bayesian blocks over the interval of a burst. In this work we calculated τ_{bb} in a similar manner as in Lin et al. (2020a), but with a temporal resolution of 1 ms. We list the τ_{bb} duration of each burst in Table 1. We find that the distribution of burst durations follows a log-Gaussian trend, as was the case for the duration distributions for SGR J1935+2154 bursts seen prior to 2019, as well as bursts from other magnetars (see, e.g., Collazzi et al. 2015). We present in the left panel of Figure 2 the duration distribution along with the best-fitting log-Gaussian function, with a mean of 169^{+18}_{-16} ms. We also formed separate duration distributions for the 2019 and 2020 episodes and fit them with a log-Gaussian function; we find that the 2020 bursts are slightly longer on average. The cumulative means of the burst durations from 2019 and 2020 are 121 ms and 182 ms, respectively (see Table 3 for details). In the right panel of Figure 2, we present a scatter plot of τ_{bb} versus burst time, each starting with the first burst of each episode. We find that the bursts from the 2020 episode show a significant increase in their frequency of occurrence, during 2–8 hr after the onset of the episode. Further, in the latter episode, all bursts with $\tau_{bb} > 1$ s occur within its first 10 hr.

Another measure of a burst duration, is T_{90}, that is the time interval over which the cumulative energy fluence of the burst increases from 5% to 95% of the total (Kouveliotou et al. 1993). Lin et al. (2020a) showed that the τ_{bb} is tightly correlated with T_{90} for SGR J1935+2154 bursts. Note that τ_{bb} is slightly longer, as it measures the full duration of the event while T_{90} measures 10% less, to account for background fluctuations preceding and following an event. Here we only report τ_{bb} durations.

3.2. Spectral Analysis

For each burst, we identified the NaI detectors with a ⩽50° angle between the detector zenith and the source at the time of the burst, and also not blocked by other parts of the spacecraft (using *gbmblock*). We then generated response matrices for

Table 1
The SGR J1935+2154 Burst List

ID	Burst Start Time in UTC	τ_{bb} (s)	F[a] $(10^{-7}\ \mathrm{erg\ cm}^{-2})$	E_{peak} (keV)	Γ	C-Stat/DoF[b]	kT_{low} (keV)	kT_{high} (keV)	C-Stat/DoF[c]
				2019					
1^T	Oct 4 09:00:53.609	0.095	0.74 ± 0.05	$26.48^{+3.21}_{-2.84}$	$\cdots$	207.96/201	$\cdots$	$\cdots$	$\cdots$
2^T	Nov 4 01:20:24.034	0.092	1.05 ± 0.06	$\cdots$	$\cdots$	$\cdots$	$4.06^{+0.49}_{-0.48}$	$12.66^{+1.67}_{-1.39}$	216.52/198
3^T	Nov 4 02:53:31.369	0.035	1.47 ± 0.06	$24.69^{+1.68}_{-1.94}$	$-0.68^{+0.29}_{-0.27}$	286.03/270	$3.94^{+0.72}_{-0.75}$	$9.90^{+1.23}_{-0.93}$	289.27/269
4^T	Nov 4 04:26:55.855	0.074	1.17 ± 0.06	$26.36^{+1.51}_{-1.58}$	$-0.14^{+0.44}_{-0.39}$	191.97/199	$5.74^{+0.45}_{-0.52}$	$15.31^{+5.11}_{-3.30}$	186.41/198
5	Nov 4 07:20:33.684	0.100	0.48 ± 0.05	$24.86^{+4.28}_{-3.65}$	$\cdots$	308.87/266	$\cdots$	$\cdots$	$\cdots$
6	Nov 4 08:56:15.943	0.043	0.17 ± 0.03	$\cdots$	$\cdots$	$\cdots$	$6.11^{+0.84}_{-0.73}$	$\cdots$	220.52/201
7^T	Nov 4 09:17:53.492	0.321	5.89 ± 0.13	$28.76^{+0.90}_{-0.93}$	$-0.62^{+0.14}_{-0.14}$	332.12/268	$4.57^{+0.27}_{-0.27}$	$11.76^{+0.62}_{-0.55}$	326.49/267
8^T	Nov 4 10:44:26.231	0.195	22.94 ± 0.23	$32.89^{+0.29}_{-0.29}$	$0.49^{+0.08}_{-0.07}$	268.16/199	$5.38^{+0.38}_{-0.38}$	$10.40^{+0.35}_{-0.30}$	269.50/198
9^T	Nov 4 12:38:38.534	0.072	2.82 ± 0.09	$26.02^{+0.85}_{-0.88}$	$0.12^{+0.27}_{-0.25}$	232.05/200	$4.97^{+0.57}_{-0.57}$	$10.06^{+1.62}_{-1.04}$	228.29/199
10^T	Nov 4 15:36:47.402	0.321	1.23 ± 0.08	$\cdots$	$\cdots$	$\cdots$	$3.66^{+0.58}_{-0.54}$	$11.89^{+1.37}_{-1.17}$	356.40/336
11	Nov 4 19:09:01.727	0.038	0.29 ± 0.04	$23.85^{+5.61}_{-4.60}$	$\cdots$	120.25/133	$\cdots$	$\cdots$	$\cdots$
12	Nov 4 20:01:41.871	0.127	0.46 ± 0.05	$\cdots$	$\cdots$	$\cdots$	$3.95^{+0.65}_{-0.59}$	$13.77^{+2.78}_{-2.23}$	301.79/264
13	Nov 4 20:13:42.537	0.140	0.61 ± 0.07	$42.00^{+8.16}_{-6.62}$	$\cdots$	210.03/200	$\cdots$	$\cdots$	$\cdots$
14^T	Nov 4 20:29:39.804	0.128	1.37 ± 0.08	$27.80^{+1.96}_{-1.96}$	$-0.18^{+0.51}_{-0.46}$	172.31/133	$\cdots$	$\cdots$	$\cdots$
15	Nov 4 23:16:49.544	0.024	0.25 ± 0.03	$\cdots$	$\cdots$	$\cdots$	$9.71^{+0.85}_{-0.78}$	$\cdots$	243.89/267
16^T	Nov 4 23:48:01.336	0.225	3.07 ± 0.11	$\cdots$	$\cdots$	$\cdots$	$3.98^{+0.33}_{-0.33}$	$12.15^{+1.10}_{-0.97}$	248.05/199
17	Nov 5 00:33:02.781	0.881	1.17 ± 0.22	$\cdots$	$-2.293^{+0.254}_{-0.298}$	71.775/65	$\cdots$	$\cdots$	$\cdots$
18^T	Nov 5 06:11:08.595	0.786	80.42 ± 0.57	$40.55^{+0.24}_{-0.24}$	$0.55^{+0.05}_{-0.05}$	362.53/132	$8.21^{+0.22}_{-0.23}$	$15.39^{+0.68}_{-0.60}$	337.39/131
19^T	Nov 5 07:17:17.705	0.194	0.91 ± 0.08	$\cdots$	$\cdots$	$\cdots$	$4.06^{+0.43}_{-0.40}$	$19.75^{+3.69}_{-2.98}$	197.99/198
20	Nov 14 00:30:46.836	0.081	0.24 ± 0.04	$\cdots$	$\cdots$	$\cdots$	$9.00^{+1.28}_{-1.14}$	$\cdots$	225.80/200
21^T	Nov 14 19:50:42.295	0.024	0.55 ± 0.04	$\cdots$	$\cdots$	$\cdots$	$4.19^{+0.56}_{-0.54}$	$13.56^{+2.28}_{-1.80}$	213.79/199
22^T	Nov 15 20:48:41.297	0.037	0.79 ± 0.06	$\cdots$	$\cdots$	$\cdots$	$3.76^{+0.42}_{-0.38}$	$14.04^{+2.07}_{-1.71}$	128.83/130
				2020					
23^T	Apr 10 09:43:54.273	0.171	27.46 ± 0.41	$32.76^{+0.38}_{-0.38}$	$0.85^{+0.11}_{-0.11}$	127.16/65	$6.81^{+0.70}_{-0.92}$	$11.05^{+2.15}_{-1.10}$	126.27/64
24^T	Apr 27 18:26:20.138	0.216	2.05 ± 0.10	$26.25^{+1.55}_{-1.61}$	$-0.36^{+0.37}_{-0.34}$	154.10/134	$4.33^{+0.78}_{-0.74}$	$10.13^{+2.05}_{-1.27}$	153.37/133
25	Apr 27 18:31:05.770	0.244	0.76 ± 0.07	$\cdots$	$\cdots$	$\cdots$	$3.47^{+0.85}_{-1.07}$	$10.99^{+2.85}_{-2.48}$	185.00/200
26	Apr 27 18:31:25.234	0.166	1.89 ± 0.08	$23.83^{+1.70}_{-1.95}$	$-0.75^{+0.30}_{-0.28}$	240.78/201	$4.15^{+0.53}_{-0.56}$	$10.49^{+1.50}_{-1.17}$	240.93/200
27	Apr 27 18:33:53.116	0.071	0.51 ± 0.04	$\cdots$	$-2.39^{+0.13}_{-0.14}$	303.72/269	$\cdots$	$\cdots$	$\cdots$
28	Apr 27 18:34:05.700	0.422	20.11 ± 0.19	$27.29^{+0.27}_{-0.27}$	$0.23^{+0.08}_{-0.08}$	392.00/268	$5.53^{+0.19}_{-0.20}$	$10.90^{+0.57}_{-0.51}$	367.22/267
29	Apr 27 18:34:46.047	0.226	3.83 ± 0.11	$\cdots$	$\cdots$	$\cdots$	$4.45^{+0.19}_{-0.19}$	$14.30^{+1.23}_{-1.10}$	211.64/198
30	Apr 27 18:34:47.296	0.534	1.05 ± 0.10	$\cdots$	$\cdots$	$\cdots$	$3.96^{+0.58}_{-0.58}$	$13.99^{+3.34}_{-2.65}$	203.53/198
31	Apr 27 18:35:05.320	0.103	5.12 ± 0.11	$27.36^{+0.71}_{-0.73}$	$-0.24^{+0.16}_{-0.15}$	220.85/199	$4.99^{+0.34}_{-0.35}$	$11.06^{+0.84}_{-0.71}$	217.28/198
32	Apr 27 18:35:46.623	0.061	1.32 ± 0.06	$27.56^{+1.12}_{-1.12}$	$0.58^{+0.40}_{-0.37}$	188.67/199	$\cdots$	$\cdots$	$\cdots$
33	Apr 27 18:35:57.633	0.025	0.45 ± 0.04	$19.46^{+2.59}_{-2.22}$	$\cdots$	194.59/200	$\cdots$	$\cdots$	$\cdots$
34	Apr 27 18:36:45.376	0.014	0.28 ± 0.03	$19.26^{+2.86}_{-2.41}$	$\cdots$	247.99/267	$\cdots$	$\cdots$	$\cdots$
35^T	Apr 27 18:36:46.007	0.346	19.42 ± 0.20	$29.26^{+0.34}_{-0.35}$	$-0.12^{+0.08}_{-0.07}$	364.99/266	$4.97^{+0.23}_{-0.23}$	$10.76^{+0.37}_{-0.35}$	374.53/265
36	Apr 27 18:38:20.206	0.105	0.93 ± 0.06	$\cdots$	$\cdots$	$\cdots$	$4.03^{+0.33}_{-0.31}$	$17.67^{+2.89}_{-2.45}$	423.22/332
37	Apr 27 18:38:53.689	0.250	1.81 ± 0.08	$\cdots$	$\cdots$	$\cdots$	$4.66^{+0.33}_{-0.35}$	$17.14^{+2.66}_{-2.31}$	351.02/332
38	Apr 27 18:39:09.331	0.035	0.19 ± 0.03	$\cdots$	$-2.11^{+0.19}_{-0.19}$	320.11/334	$\cdots$	$\cdots$	$\cdots$
39	Apr 27 18:40:15.043	0.456	1.15 ± 0.09	$23.65^{+3.49}_{-3.06}$	$\cdots$	305.48/266	$\cdots$	$\cdots$	$\cdots$
40	Apr 27 18:40:32.031	1.353	6.16 ± 0.18	$24.74^{+1.51}_{-1.74}$	$-1.07^{+0.19}_{-0.18}$	375.27/265	$4.19^{+0.28}_{-0.28}$	$11.71^{+0.93}_{-0.80}$	371.44/264
41	Apr 27 18:42:40.816	0.031	0.35 ± 0.03	$14.01^{+2.52}_{-2.05}$	$\cdots$	173.11/199	$\cdots$	$\cdots$	$\cdots$
42	Apr 27 18:42:50.652	0.316	8.17 ± 0.15	$23.44^{+0.85}_{-0.92}$	$-0.81^{+0.14}_{-0.13}$	274.17/198	$4.86^{+0.18}_{-0.19}$	$12.86^{+0.87}_{-0.79}$	256.98/197
43	Apr 27 18:44:08.209	0.077	0.34 ± 0.06	$\cdots$	$\cdots$	$\cdots$	$2.98^{+0.78}_{-0.62}$	$14.69^{+4.01}_{-3.07}$	139.07/130
44	Apr 27 18:46:08.767	0.206	3.86 ± 0.13	$25.91^{+1.13}_{-1.20}$	$-0.40^{+0.26}_{-0.25}$	140.86/131	$5.06^{+0.48}_{-0.59}$	$11.75^{+1.93}_{-1.61}$	140.74/130
45	Apr 27 18:46:39.414	1.651	9.70 ± 0.26	$25.08^{+0.86}_{-0.90}$	$-0.40^{+0.22}_{-0.21}$	185.19/131	$4.98^{+0.40}_{-1.13}$	$11.83^{+2.10}_{-2.92}$	185.35/130
46^T	Apr 27 18:47:05.754	0.155	11.78 ± 0.20	$31.86^{+0.47}_{-0.47}$	$0.56^{+0.14}_{-0.13}$	165.91/131	$5.21^{+0.67}_{-0.64}$	$9.92^{+0.64}_{-0.45}$	165.95/130
47	Apr 27 18:48:38.675	0.243	1.69 ± 0.10	$\cdots$	$\cdots$	$\cdots$	$4.10^{+0.60}_{-0.68}$	$11.84^{+2.48}_{-1.95}$	129.68/130
48	Apr 27 18:49:28.034	0.368	6.83 ± 0.17	$23.06^{+1.05}_{-1.16}$	$-0.75^{+0.19}_{-0.18}$	189.01/131	$4.58^{+0.26}_{-0.27}$	$11.66^{+1.06}_{-0.93}$	181.99/130
49	Apr 27 18:50:28.665	0.025	0.27 ± 0.03	$\cdots$	$\cdots$	$\cdots$	$6.14^{+0.68}_{-0.60}$	$\cdots$	118.79/132
50	Apr 27 18:50:49.460	0.035	0.26 ± 0.04	$\cdots$	$\cdots$	$\cdots$	$7.38^{+0.85}_{-0.78}$	$\cdots$	107.17/132
51	Apr 27 18:55:44.155	0.072	2.65 ± 0.12	$28.91^{+1.79}_{-1.95}$	$-0.62^{+0.29}_{-0.27}$	132.47/131	$5.26^{+0.49}_{-0.50}$	$13.46^{+1.82}_{-1.48}$	129.30/130
52	Apr 27 18:57:35.574	0.096	0.78 ± 0.08	$26.42^{+4.62}_{-3.87}$	$\cdots$	148.87/132	$\cdots$	$\cdots$	$\cdots$
53	Apr 27 18:58:45.533	0.193	0.78 ± 0.11	$\cdots$	$-2.397^{+0.193}_{-0.222}$	166/132	$\cdots$	$\cdots$	$\cdots$

Table 1
(Continued)

ID	Burst Start Time in UTC	τ_{bb} (s)	F[a] (10^{-7} erg cm^{-2})	E_{peak} (keV)	Γ	C-Stat/DoF[b]	kT_{low} (keV)	kT_{high} (keV)	C-Stat/DoF[c]
54	Apr 27 19:36:05.104	0.028	0.40 ± 0.04	⋯	⋯	⋯	$4.51^{+0.54}_{-0.49}$	$20.09^{+6.04}_{-4.21}$	207.13/199
55[T]	Apr 27 19:37:39.328	0.724	3.89 ± 0.16	⋯	⋯	⋯	$4.29^{+0.24}_{-0.24}$	$16.26^{+1.82}_{-1.63}$	238.87/199
56	Apr 27 19:43:44.537	0.436	38.42 ± 0.24	$32.02^{+0.17}_{-0.17}$	$0.78^{+0.05}_{-0.05}$	591.99/337	$6.91^{+0.23}_{-0.27}$	$11.47^{+0.70}_{-0.58}$	583.95/336
57	Apr 27 19:45:00.478	0.101	0.51 ± 0.05	⋯	⋯	⋯	$1.94^{+0.46}_{-0.38}$	$9.69^{+1.22}_{-1.02}$	379.07/336
58	Apr 27 19:55:32.325	0.041	0.23 ± 0.03	⋯	⋯	⋯	$5.35^{+0.52}_{-0.47}$	⋯	179.42/203
59[T]	Apr 27 20:01:45.681	0.483	5.08 ± 0.15	$26.24^{+1.06}_{-1.11}$	$-0.50^{+0.22}_{-0.21}$	155.70/134	$4.55^{+0.39}_{-0.41}$	$10.92^{+1.11}_{-0.94}$	154.88/133
60	Apr 27 20:07:20.319	0.382	0.79 ± 0.10	$56.43^{+14.00}_{-10.20}$	⋯	219.88/202	⋯	⋯	⋯
61[T]	Apr 27 20:13:38.263	0.055	0.52 ± 0.04	⋯	⋯	⋯	$4.29^{+1.16}_{-1.13}$	$10.83^{+2.52}_{-1.59}$	328.39/332
62	Apr 27 20:14:51.396	0.051	1.38 ± 0.06	$27.73^{+1.61}_{-1.75}$	$-0.54^{+0.29}_{-0.28}$	267.85/265	$4.44^{+0.57}_{-0.54}$	$11.07^{+1.24}_{-0.96}$	266.26/264
63	Apr 27 20:15:20.583	1.282	189.77 ± 0.67	$34.25^{+0.10}_{-0.10}$	$0.56^{+0.03}_{-0.03}$	639.98/247	$6.61^{+0.17}_{-0.15}$	$11.77^{+0.25}_{-0.21}$	630.40/246
64	Apr 27 20:16:15.285	0.030	0.32 ± 0.03	$21.49^{+3.38}_{-2.93}$	⋯	271.06/266	⋯	⋯	⋯
65	Apr 27 20:17:09.139	0.110	0.71 ± 0.06	⋯	⋯	⋯	$3.94^{+0.49}_{-0.53}$	$12.32^{+2.51}_{-2.05}$	226.45/197
66	Apr 27 20:17:27.317	0.064	0.58 ± 0.05	⋯	⋯	⋯	$5.09^{+0.83}_{-0.93}$	$18.29^{+6.82}_{-5.25}$	171.55/197
67	Apr 27 20:17:50.343	1.422	2.20 ± 0.18	$36.27^{+6.13}_{-5.03}$	⋯	275.72/199	⋯	⋯	⋯
68	Apr 27 20:17:58.442	0.078	1.15 ± 0.06	⋯	⋯	⋯	$4.42^{+0.66}_{-0.76}$	$11.19^{+2.25}_{-1.70}$	219.72/197
69	Apr 27 20:18:09.130	0.836	0.36 ± 0.09	⋯	⋯	⋯	$7.84^{+1.83}_{-1.44}$	⋯	214.22/199
70	Apr 27 20:19:23.068	0.030	0.31 ± 0.04	⋯	$-2.71^{+0.22}_{-0.25}$	121.56/132	⋯	⋯	⋯
71	Apr 27 20:19:47.631	0.849	1.16 ± 0.17	⋯	$-1.92^{+0.17}_{-0.18}$	131.42/132	⋯	⋯	⋯
72	Apr 27 20:19:49.430	0.232	4.09 ± 0.14	$23.83^{+1.55}_{-1.83}$	$-0.93^{+0.25}_{-0.24}$	151.93/131	$4.97^{+0.36}_{-0.43}$	$14.06^{+2.35}_{-2.10}$	147.39/130
73	Apr 27 20:20:44.640	0.335	0.74 ± 0.09	$23.79^{+5.85}_{-4.58}$	⋯	121.99/132	⋯	⋯	⋯
74	Apr 27 20:21:51.841	0.578	1.63 ± 0.14	⋯	⋯	⋯	$3.91^{+0.49}_{-0.43}$	$16.33^{+2.44}_{-2.10}$	179.22/130
75	Apr 27 20:21:55.136	0.549	9.34 ± 0.20	$23.67^{+0.75}_{-0.80}$	$-0.48^{+0.18}_{-0.17}$	166.74/131	$4.81^{+0.32}_{-0.39}$	$11.46^{+1.52}_{-1.32}$	162.53/130
76	Apr 27 20:25:53.415	0.400	1.55 ± 0.14	⋯	⋯	⋯	$4.34^{+0.53}_{-0.49}$	$16.82^{+3.52}_{-2.72}$	148.97/130
77[T]	Apr 27 21:14:45.605	0.265	10.15 ± 0.15	$30.93^{+0.47}_{-0.48}$	$0.01^{+0.10}_{-0.10}$	366.35/268	$6.12^{+0.30}_{-0.31}$	$12.78^{+1.01}_{-0.78}$	363.69/267
78	Apr 27 21:15:36.398	0.383	6.47 ± 0.13	$27.39^{+0.78}_{-0.81}$	$-0.53^{+0.15}_{-0.14}$	309.75/268	$4.84^{+0.27}_{-0.28}$	$11.70^{+0.79}_{-0.70}$	305.47/267
79	Apr 27 21:20:55.561	0.089	0.96 ± 0.05	⋯	⋯	⋯	$4.16^{+0.42}_{-0.48}$	$10.23^{+1.93}_{-1.56}$	409.23/336
80	Apr 27 21:20:58.670	0.187	0.77 ± 0.06	⋯	⋯	⋯	$4.34^{+0.44}_{-0.41}$	$16.00^{+3.13}_{-2.52}$	396.53/336
81	Apr 27 21:24:05.936	0.050	0.42 ± 0.04	⋯	$-2.17^{+0.14}_{-0.15}$	221.69/203	⋯	⋯	⋯
82	Apr 27 21:25:01.037	0.060	0.39 ± 0.04	$24.03^{+3.83}_{-3.19}$	⋯	190.57/203	⋯	⋯	⋯
83	Apr 27 21:27:25.367	0.246	0.47 ± 0.07	⋯	$-2.15^{+0.17}_{-0.19}$	242.45/203	⋯	⋯	⋯
84[T]	Apr 27 21:43:06.346	0.163	1.66 ± 0.08	$17.05^{+1.50}_{-1.35}$	⋯	152.64/134	⋯	⋯	⋯
85	Apr 27 21:48:44.062	0.283	6.59 ± 0.12	$23.76^{+0.66}_{-0.70}$	$-0.36^{+0.15}_{-0.15}$	304.76/266	$4.31^{+0.29}_{-0.31}$	$9.57^{+0.61}_{-0.53}$	304.16/265
86	Apr 27 21:57:03.989	0.029	0.23 ± 0.04	⋯	$-2.70^{+0.27}_{-0.32}$	147.94/132	⋯	⋯	⋯
87[T]	Apr 27 21:59:22.528	0.239	14.88 ± 0.23	$32.32^{+0.48}_{-0.48}$	$0.22^{+0.12}_{-0.11}$	143.43/131	$5.21^{+0.41}_{-0.41}$	$10.81^{+0.53}_{-0.44}$	142.45/130
88	Apr 27 22:47:05.343	0.017	0.20 ± 0.03	$28.94^{+8.85}_{-6.51}$	⋯	185.79/201	⋯	⋯	⋯
89[T]	Apr 27 22:55:19.911	0.266	1.97 ± 0.10	⋯	⋯	⋯	$5.17^{+0.47}_{-0.47}$	$17.42^{+3.34}_{-2.56}$	228.90/201
90	Apr 27 23:02:53.488	0.261	7.10 ± 0.13	$22.37^{+0.67}_{-0.72}$	$-0.52^{+0.15}_{-0.14}$	252.34/202	$4.26^{+0.24}_{-0.25}$	$9.80^{+0.63}_{-0.55}$	249.33/201
91[T]	Apr 27 23:06:06.135	0.166	2.02 ± 0.08	$24.68^{+1.53}_{-1.71}$	$-0.67^{+0.28}_{-0.26}$	185.58/202	$4.50^{+0.38}_{-0.37}$	$11.50^{+1.30}_{-1.09}$	180.17/201
92[T]	Apr 27 23:25:04.349	0.502	1.75 ± 0.11	⋯	$-2.22^{+0.08}_{-0.09}$	352.76/266	⋯	⋯	⋯
93	Apr 27 23:27:46.293	0.068	3.23 ± 0.09	$29.05^{+0.76}_{-0.77}$	$0.45^{+0.25}_{-0.23}$	207.07/198	$6.26^{+0.49}_{-0.67}$	$12.27^{+2.74}_{-1.92}$	203.33/197
94[T]	Apr 27 23:42:41.143	0.053	1.93 ± 0.10	$28.75^{+1.67}_{-1.77}$	$-0.11^{+0.40}_{-0.37}$	153.33/131	$3.99^{+0.57}_{-0.63}$	$9.83^{+0.82}_{-0.76}$	150.21/130
95	Apr 27 23:44:31.818	0.322	14.49 ± 0.30	$38.69^{+0.64}_{-0.63}$	$0.84^{+0.17}_{-0.16}$	189.12/131	$8.56^{+0.30}_{-0.30}$	$18.98^{+2.47}_{-1.92}$	158.25/130
96[T]	Apr 28 00:19:44.173	0.151	1.11 ± 0.06	$20.62^{+2.17}_{-1.94}$	⋯	251.63/201	⋯	⋯	⋯
97	Apr 28 00:23:04.763	0.113	0.69 ± 0.06	⋯	⋯	⋯	$3.01^{+0.54}_{-0.46}$	$10.19^{+1.39}_{-1.11}$	191.30/199
98	Apr 28 00:24:30.311	0.236	34.49 ± 0.26	$32.72^{+0.21}_{-0.21}$	$0.66^{+0.06}_{-0.06}$	409.07/268	$6.46^{+0.34}_{-0.37}$	$11.02^{+0.59}_{-0.48}$	410.88/267
99	Apr 28 00:25:43.946	0.042	0.25 ± 0.03	⋯	⋯	⋯	$2.68^{+0.58}_{-0.60}$	$11.57^{+3.65}_{-3.02}$	267.66/267
100	Apr 28 00:37:36.160	0.115	0.63 ± 0.05	$25.87^{+3.89}_{-3.32}$	⋯	214.84/203	⋯	⋯	⋯
101[T]	Apr 28 00:39:39.565	0.659	2.29 ± 0.11	⋯	⋯	⋯	$3.67^{+0.49}_{-0.50}$	$10.14^{+1.92}_{-1.38}$	209.97/201
102	Apr 28 00:40:33.077	0.689	4.28 ± 0.13	⋯	⋯	⋯	$3.88^{+0.22}_{-0.22}$	$11.30^{+1.09}_{-0.97}$	268.16/201
103	Apr 28 00:41:32.148	0.437	13.76 ± 0.19	$27.22^{+0.50}_{-0.51}$	$-0.44^{+0.10}_{-0.10}$	271.86/202	$5.10^{+0.24}_{-0.29}$	$11.71^{+0.71}_{-0.70}$	286.28/201
104	Apr 28 00:43:24.784	0.846	6.52 ± 0.15	$22.58^{+0.58}_{-0.60}$	$0.26^{+0.23}_{-0.23}$	278.24/202	$4.66^{+0.34}_{-0.38}$	$9.18^{+1.37}_{-0.97}$	271.59/201
105	Apr 28 00:44:08.210	1.275	70.82 ± 0.45	$38.45^{+0.21}_{-0.21}$	$0.29^{+0.04}_{-0.04}$	569.03/202	$6.35^{+0.22}_{-0.24}$	$12.80^{+0.28}_{-0.27}$	597.48/201
106	Apr 28 00:45:31.098	0.107	0.86 ± 0.06	$21.21^{+2.33}_{-2.05}$	⋯	213.69/203	⋯	⋯	⋯
107	Apr 28 00:46:00.034	0.798	6.05 ± 0.18	$23.09^{+1.68}_{-1.96}$	$-1.19^{+0.17}_{-0.16}$	207.89/134	$5.17^{+0.22}_{-0.22}$	$17.32^{+1.78}_{-1.54}$	188.72/133
108	Apr 28 00:46:06.394	0.176	0.87 ± 0.07	$22.12^{+3.19}_{-2.74}$	⋯	156.89/135	⋯	⋯	⋯
109	Apr 28 00:46:20.179	0.851	46.93 ± 0.43	$38.72^{+0.31}_{-0.31}$	$0.27^{+0.06}_{-0.06}$	240.75/134	$6.85^{+0.31}_{-0.29}$	$13.80^{+0.62}_{-0.49}$	242.40/133
110	Apr 28 00:46:23.528	0.843	2.71 ± 0.14	$17.90^{+1.00}_{-1.20}$	$0.35^{+0.72}_{-0.59}$	138.48/134	⋯	⋯	⋯

Table 1
(Continued)

ID	Burst Start Time in UTC	τ_{bb} (s)	F^a (10^{-7} erg cm^{-2})	E_{peak} (keV)	Γ	C-Stat/DoF^b	kT_{low} (keV)	kT_{high} (keV)	C-Stat/DoF^c
111	Apr 28 00:46:43.072	0.503	3.82 ± 0.14	$23.23^{+1.03}_{-1.09}$	$-0.19^{+0.32}_{-0.30}$	146.59/134	$4.32^{+0.52}_{-0.55}$	$9.35^{+1.63}_{-1.09}$	144.69/133
112	Apr 28 00:47:24.957	0.239	0.84 ± 0.08	$21.07^{+3.34}_{-2.84}$	$\cdots$	142.74/135	$\cdots$	$\cdots$	$\cdots$
113	Apr 28 00:47:57.536	0.260	1.50 ± 0.09	$21.31^{+1.33}_{-1.38}$	$0.29^{+0.61}_{-0.56}$	141.30/134	$\cdots$	$\cdots$	$\cdots$
114	Apr 28 00:48:44.833	0.443	1.88 ± 0.11	$\cdots$	$\cdots$	$\cdots$	$4.58^{+0.26}_{-0.27}$	$16.25^{+3.91}_{-3.11}$	216.35/200
115	Apr 28 00:48:49.098	0.597	8.17 ± 0.17	$31.17^{+0.93}_{-0.94}$	$-0.75^{+0.12}_{-0.12}$	265.81/201	$5.46^{+0.25}_{-0.25}$	$14.91^{+1.04}_{-0.91}$	260.72/200
116	Apr 28 00:49:00.270	2.607	2.85 ± 0.21	$\cdots$	$\cdots$	$\cdots$	$3.63^{+0.40}_{-0.39}$	$11.76^{+1.93}_{-1.59}$	356.21/200
117	Apr 28 00:49:06.479	0.027	0.21 ± 0.03	$15.12^{+3.23}_{-2.58}$	$\cdots$	150.25/202	$\cdots$	$\cdots$	$\cdots$
118	Apr 28 00:49:16.609	0.313	3.94 ± 0.11	$20.64^{+0.88}_{-0.99}$	$-0.40^{+0.29}_{-0.26}$	218.99/201	$4.18^{+0.19}_{-0.21}$	$14.39^{+2.22}_{-1.92}$	195.58/200
119	Apr 28 00:49:22.392	0.091	0.64 ± 0.04	$14.28^{+1.88}_{-1.60}$	$\cdots$	241.30/202	$\cdots$	$\cdots$	$\cdots$
120	Apr 28 00:49:27.008	0.347	0.64 ± 0.07	$21.46^{+4.71}_{-3.83}$	$\cdots$	270.72/202	$\cdots$	$\cdots$	$\cdots$
121^T	Apr 28 00:49:45.895	1.164	2.88 ± 0.16	$\cdots$	$\cdots$	$\cdots$	$3.97^{+0.25}_{-0.25}$	$16.98^{+2.83}_{-2.43}$	259.29/197
122	Apr 28 00:50:01.012	0.499	3.64 ± 0.11	$21.34^{+0.76}_{-0.82}$	$0.08^{+0.31}_{-0.30}$	173.68/201	$4.65^{+0.35}_{-0.46}$	$9.82^{+2.14}_{-1.60}$	170.29/200
123	Apr 28 00:50:21.993	0.021	0.18 ± 0.02	$19.73^{+5.26}_{-3.98}$	$\cdots$	162.99/202	$\cdots$	$\cdots$	$\cdots$
124	Apr 28 00:50:41.835	0.405	0.63 ± 0.09	$33.78^{+9.89}_{-7.48}$	$\cdots$	212.63/202	$\cdots$	$\cdots$	$\cdots$
125	Apr 28 00:51:35.912	0.069	0.77 ± 0.04	$16.16^{+1.60}_{-1.43}$	$\cdots$	197.26/202	$\cdots$	$\cdots$	$\cdots$
126	Apr 28 00:51:55.444	0.132	0.86 ± 0.05	$13.62^{+1.34}_{-1.20}$	$\cdots$	204.48/202	$\cdots$	$\cdots$	$\cdots$
127	Apr 28 00:52:06.141	0.380	0.75 ± 0.08	$28.08^{+5.15}_{-4.30}$	$\cdots$	194.49/202	$\cdots$	$\cdots$	$\cdots$
128	Apr 28 00:54:57.448	0.172	4.45 ± 0.09	$24.06^{+0.70}_{-0.71}$	$-0.24^{+0.18}_{-0.17}$	344.14/268	$4.69^{+0.32}_{-0.58}$	$10.09^{+0.97}_{-1.14}$	341.98/267
129	Apr 28 00:56:49.646	0.328	1.44 ± 0.09	$\cdots$	$\cdots$	$\cdots$	$3.68^{+0.56}_{-0.59}$	$9.46^{+2.12}_{-1.46}$	243.73/198
130^T	Apr 28 01:04:03.146	0.062	0.77 ± 0.05	$\cdots$	$\cdots$	$\cdots$	$4.15^{+0.50}_{-0.56}$	$11.40^{+2.72}_{-2.06}$	225.28/197
131^T	Apr 28 02:00:11.518	0.234	1.70 ± 0.08	$\cdots$	$\cdots$	$\cdots$	$2.91^{+0.42}_{-0.42}$	$9.57^{+0.96}_{-0.81}$	312.10/267
132	Apr 28 02:27:24.905	0.026	0.20 ± 0.03	$31.56^{+8.14}_{-6.35}$	$\cdots$	182.16/202	$\cdots$	$\cdots$	$\cdots$
133	Apr 28 03:32:00.607	0.130	0.61 ± 0.07	$\cdots$	$\cdots$	$\cdots$	$2.72^{+0.59}_{-0.51}$	$14.99^{+2.30}_{-1.99}$	231.65/199
134^T	Apr 28 03:47:52.140	0.143	2.00 ± 0.07	$20.79^{+1.16}_{-1.13}$	$-0.42^{+0.33}_{-0.31}$	300.64/270	$\cdots$	$\cdots$	$\cdots$
135^T	Apr 28 04:09:47.317	0.110	1.89 ± 0.06	$27.48^{+1.47}_{-1.61}$	$-0.68^{+0.24}_{-0.23}$	358.72/333	$4.63^{+0.44}_{-0.44}$	$11.69^{+1.18}_{-0.97}$	358.28/332
136^T	Apr 28 05:56:30.570	0.249	2.21 ± 0.12	$27.30^{+1.43}_{-1.43}$	$0.21^{+0.47}_{-0.43}$	140.81/131	$5.25^{+1.26}_{-2.60}$	$10.09^{+7.02}_{-2.41}$	141.30/130
137^T	Apr 28 09:51:04.838	0.240	2.35 ± 0.10	$\cdots$	$\cdots$	$\cdots$	$4.12^{+0.28}_{-0.30}$	$11.49^{+3.19}_{-1.99}$	208.03/199
138	Apr 29 11:13:57.687	0.485	0.88 ± 0.12	$\cdots$	$-1.51^{+0.14}_{-0.15}$	252.61/201	$\cdots$	$\cdots$	$\cdots$
139^T	Apr 29 20:47:27.860	0.282	41.61 ± 0.34	$34.35^{+0.216}_{-0.215}$	$0.834^{+0.0628}_{-0.0621}$	309.9/200	$6.006^{+0.531}_{-0.589}$	$10.31^{+0.405}_{-0.324}$	313.89/199
140^T	May 3 23:25:13.437	0.186	13.69 ± 0.16	$30.24^{+0.36}_{-0.36}$	$0.11^{+0.09}_{-0.09}$	321.96/270	$5.69^{+0.26}_{-0.28}$	$11.45^{+0.58}_{-0.52}$	320.24/269
141	May 5 02:54:05.299	0.025	0.17 ± 0.02	$21.99^{+5.84}_{-4.68}$	$\cdots$	253.91/270	$\cdots$	$\cdots$	$\cdots$
142	May 5 03:02:56.033	0.163	0.42 ± 0.06	$51.90^{+13.30}_{-9.92}$	$\cdots$	311.04/270	$\cdots$	$\cdots$	$\cdots$
143	May 9 00:39:12.747	0.013	0.30 ± 0.04	$25.10^{+5.42}_{-4.36}$	$\cdots$	111.97/132	$\cdots$	$\cdots$	$\cdots$
144^T	May 10 21:51:16.278	0.396	46.49 ± 0.67	$37.84^{+0.50}_{-0.49}$	$0.26^{+0.10}_{-0.10}$	106.37/64	$7.16^{+0.43}_{-0.45}$	$14.22^{+1.11}_{-0.87}$	103.61/63
145^T	May 19 18:32:30.295	0.688	4.66 ± 0.23	$\cdots$	$\cdots$	$\cdots$	$4.132^{+0.396}_{-0.384}$	$13.37^{+1.41}_{-1.22}$	70.726/63
146	May 19 18:57:36.305	0.033	0.17 ± 0.03	$\cdots$	$\cdots$	$\cdots$	$8.81^{+1.36}_{-1.20}$	$\cdots$	102.60/132
147^T	May 20 14:10:49.826	0.085	0.47 ± 0.05	$33.64^{+5.76}_{-4.79}$	$\cdots$	267.70/202	$\cdots$	$\cdots$	$\cdots$
148^T	May 20 21:47:07.495	0.446	5.02 ± 0.13	$24.37^{+2.03}_{-2.39}$	$-1.37^{+0.14}_{-0.13}$	254.28/202	$4.75^{+0.22}_{-0.22}$	$15.47^{+1.05}_{-0.95}$	249.59/201

Notes. ^{T} Bursts triggered GBM.
^{a} Fluence in 8–200 keV.
^{b} C-Stat for the COMPT model fit or OTTB/PL fit.
^{c} C-Stat for the BB+BB model fit or BB fit.

(This table is available in machine-readable form.)

each detector using the position of SGR J1935+2154 at the start time of each burst with the *gbmrsp* software. We performed spectral modeling with the RMFIT suite, using Cash statistics (Cash 1979).

The time-integrated burst spectra were extracted using the τ_{bb} interval and were fit with two continuum models that represent magnetar burst spectra the best: the sum of two blackbody functions (BB+BB) and the Comptonized model (COMPT).[7] Three other simpler models were also fit to the data

---

[7] The Comptonized model is an exponentially cutoff power law with the photon number flux $\mathcal{F} \propto E^{\Gamma} \exp[-E(2 + \Gamma)/E_{peak}]$, where E_{peak} is the peak energy and Γ is the photon index.

when neither the BB+BB nor the COMPT model parameters could be well constrained (Lin et al. 2020a). These were power law (PL), optically thin thermal bremsstrahlung (OTTB), and single blackbody (BB). In Table 4, we summarize the performance of these models in fitting the SGR J1935 +2154 burst spectra. In Table 1, we tabulated the best-fit model parameters, fit statistics, and their fluence (8 − 200 keV).

The left panel of Figure 3 shows the distributions of both the low and high BB temperatures for the 90 bursts that were adequately represented with the BB+BB model. The low BB temperature follows a Gaussian trend with the best-fit mean

Table 2
SGR J1935+2154 Activation Intervals

Episode	Start Date	End Date	Triggered (Untriggered) Events	Total Number	Burst Fluence[a] $(10^{-7} \, \mathrm{erg \, cm^{-2}})$	Burst Energy[a,b] $(10^{40} \, \mathrm{erg})$
1	2019 Nov 4	2019 Nov 15	13(8)	21	127.4 ± 0.7	12.3 ± 0.1
2	2020 Apr 27	2020 May 20[d]	28(97)	125[c]	813.3 ± 1.7	78.6 ± 0.2
all	2019 Oct 4	2020 May 20[d]	43(105)	148[c]	968.8 ± 1.9	93.6 ± 0.2

Notes.
[a] Values are the sum of fluence and energy in 8−200 keV, respectively, for all bursts in each episode.
[b] Assuming a distance of 9 kpc to SGR J1935+2154.
[c] Does not include the bursts from the burst forest.
[d] The burst search was performed until 2020 May 31. GBM did not trigger on any burst from SGR J1935+2154 after that time. Additional single, untriggered bursts after the end of the 2020 active episodes will not affect our results significantly.
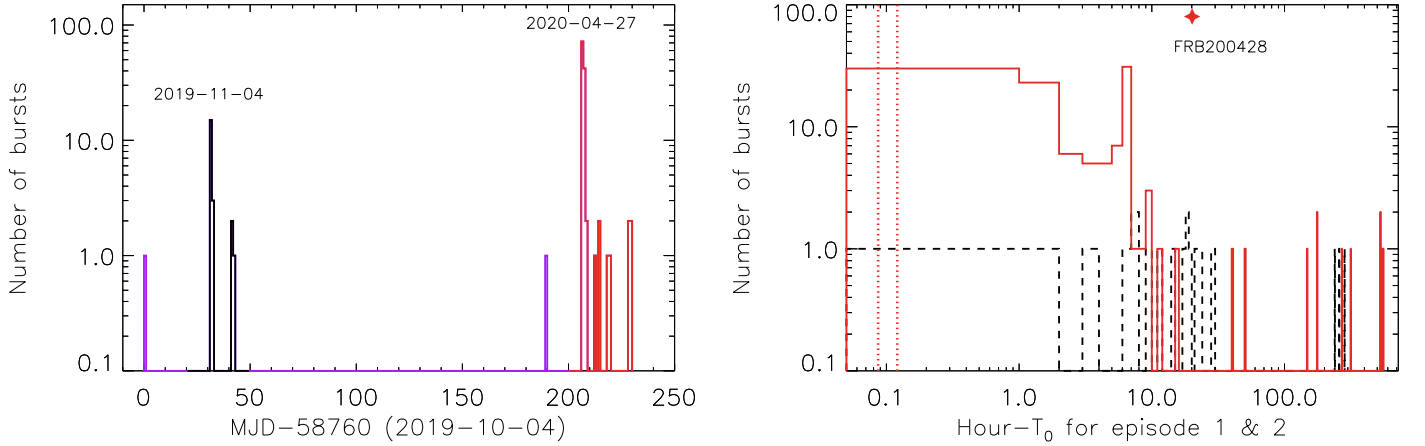
Figure 1. Left: the burst history of SGR J1935+2154 in 1 day time bins from 2019 October 4 to 2020 May 20. The bursts in episodes 1 and 2 are highlighted in black and red, respectively. Two bursts in purple are isolated events, occurring prior to each episode. Right: the number of bursts per hour for the first (dashed black line) and second (solid red line) active episodes, respectively. The red dotted lines mark the start and stop times of the burst forest not included in this work. The red star shows the relative time of FRB 200428 during the second active episode. We assign black and red in all forthcoming figures to the first and second active episodes, respectively.
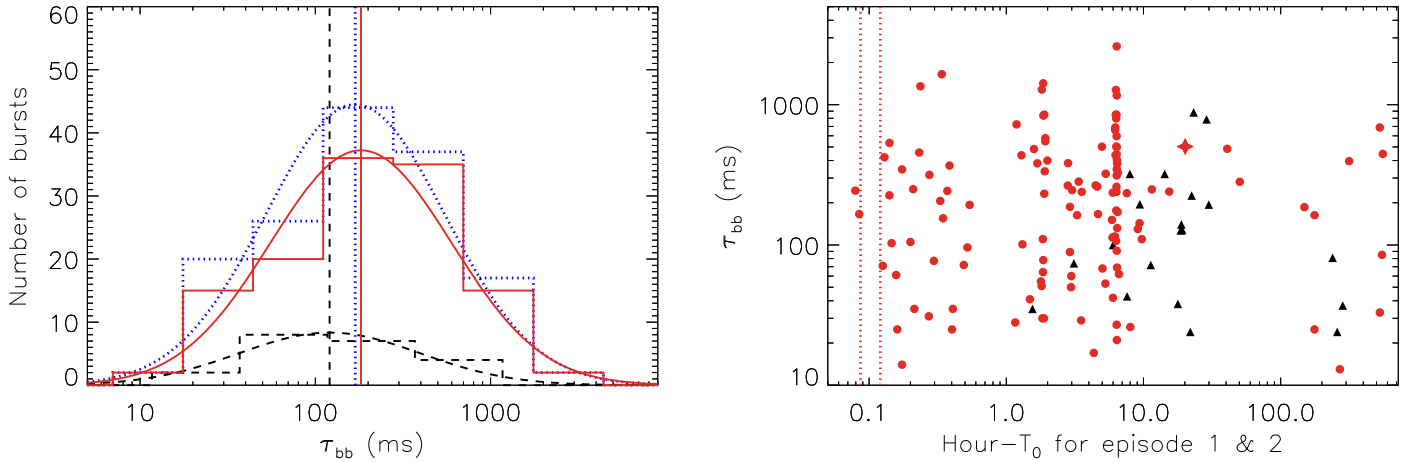
Figure 2. Left: the distribution of τ_{bb} for the whole sample (blue dotted histogram), and for active episodes 1 and 2 (dashed black and solid red histograms, respectively). The best-fit log-Gaussian functions and corresponding mean values are overplotted with the same color and style curves and vertical lines, respectively. Right: the scatter plot of τ_{bb} vs. their start time with respect to the first burst of active episodes 1 (black triangles) and 2 (red dots). The dotted lines mark the start and stop times of the burst forest. The duration and occurrence time of the X-ray burst associated with FRB 200428 is also marked with a red star.

value of 4.5 ± 0.1 keV. The distribution of the high BB temperature is asymmetric due to its overlap with the low BB component and is best fit with a truncated Gaussian function with a lower cutoff at the highest low BB temperature (8.2 keV), resulting in a mean value of 10.7 ± 1.3 keV. We also note here that when similar analyses were performed individually for the two burst episodes, their temperatures agreed within statistical errors, as shown in Table 3.

Next, we investigated how the best-fit model parameters and the calculated fluences correlated with each other. We present these correlations in Table 5 with the results of their power-law fits obtained from linear fits in logarithmic scale, as well as the

Table 3
Results of the Gaussian Fits to The Temporal and Spectral Parameter Distributions of SGR J1935+2154 Bursts

Parameter	Episode 1			Episode 2		
	μ	σ	χ^2_ν	μ	σ	χ^2_ν
τ_{bb}[a] (ms)	121^{+45}_{-33}	0.52 ± 0.14	0.38	182^{+22}_{-19}	0.52 ± 0.04	1.29
BB+BB kT_{low} (keV)	4.0 ± 0.7	1.0 ± 0.7	1.00	4.5 ± 0.1	1.0 ± 0.1	1.17
BB+BB kT_{high} (keV)	13.6 ± 1.3	2.6 ± 1.7	0.91	9.4 ± 2.8	4.3 ± 1.7	1.6
COMPT E_{peak} (keV)	27.0 ± 1.0	2.4 ± 0.8	1.00	26.3 ± 0.7	4.3 ± 0.6	1.69
COMPT Γ	-0.31 ± 0.89	0.89 ± 1.07	0.04	-0.10 ± 0.12	0.67 ± 0.12	0.13

Note.
[a] σ is in the logarithmic scale.

Table 4
Continuum Models Employed in Fitting SGR J1935+2154 Burst Spectra

Episode	Number of Bursts	BB+BB[a] (%)	COMPT[b] (%)	Both[c]	Simple Models[d]		
					OTTB	PL	BB
1	21	13 (62)	7 (33)	6	3	1	3
2	125	76 (61)	48 (39)	44	31	9	5
all	148	90 (61)	56 (38)	51	35	10	8

Notes.
[a] The number and percentage of bursts that can be adequately fit with the BB+BB model.
[b] The number and percentage of bursts that can be adequately fit with the COMPT model.
[c] The number of bursts that can be fit with both BB+BB and COMPT models.
[d] The number of bursts that can only be fit with simple models (OTTB, PL, or BB).
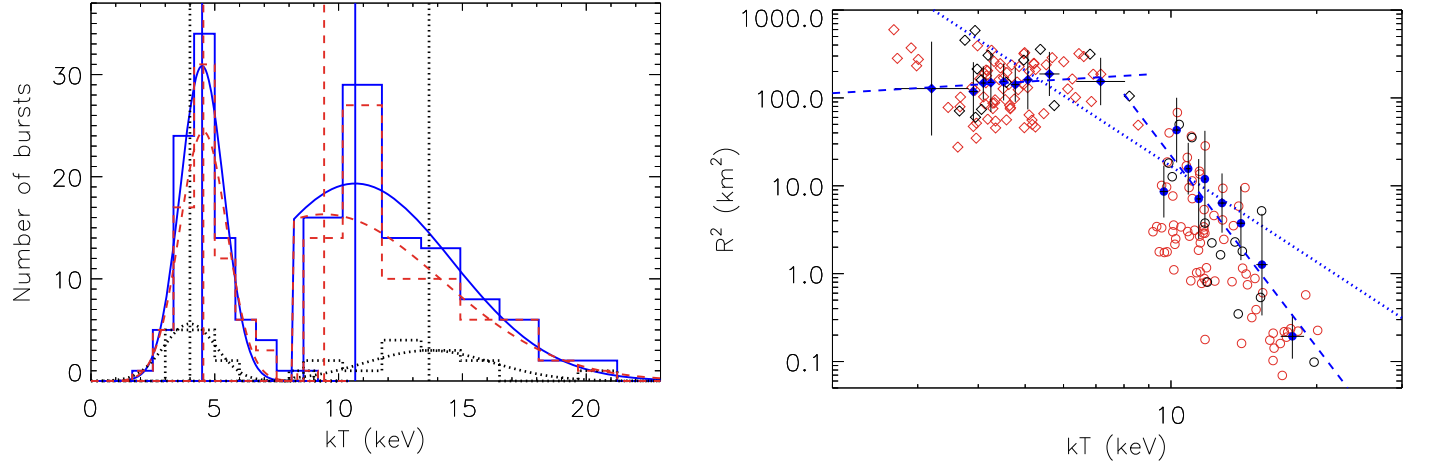
Figure 3. Left: the distributions of the low and high BB temperatures derived with the BB+BB model with the best-fit Gaussian curves and their mean values. The solid blue lines, dotted black lines, and dashed red lines represent all bursts, bursts in 2019, and bursts in 2020, respectively. Right: the emission areas (R^2) as a function of the low (diamonds) and high (circles) BB temperatures. The blue-filled symbols represent values for groups of every 10 data points. The dashed blue lines indicate the PL fit to the grouped data of each BB temperature emission region. The dotted blue line is the PL fit of both BB components in linear R^2–T space. The colors denote events in episodes 2 (red) and 1 (black).

parameters of each Spearman's rank order correlation test.[8] We find the size of the BB emitting regions (R^2) and energy fluence (F and thus luminosities) of both BB components to be strongly correlated for the 90 bursts in our sample ($R^2_{high} \propto (R^2_{low})^\alpha$, $F_{high} \propto F^\alpha_{low}$ and $L_{high} \propto L^\alpha_{low}$ in Table 5), as are the areas (R^2) and the temperatures of the two BB components ($R^2 \propto kT^\alpha$ in Table 5). The high BB temperature component was found to be inversely proportional to the emission area (the right panel of Figure 3). In contrast, the emission area of the low temperature

BB component is relatively constant across its entire temperature range. There is significant scatter in the temperatures and emission areas for both BB components in the ensembles: a power law fit to the R^2–T correlation may be highly affected by a few outliers. Accordingly, we grouped every 10 data points and performed the PL fit for each BB component on the grouped data as illustrated in the right panel of Figure 3. The fit results are listed in Table 5. Interestingly, the emission area dependence spanning both the low and high BB temperatures, $R^2 \propto (kT)^{-3.6 \pm 0.2}$, was very similar to the one corresponding to a single BB obeying the Stefan–Boltzmann law: $R^2 \propto (kT)^{-4}$. This R–T correlation for BB+BB fits is also very close to that

---

[8] We caution that artifacts may affect the results when subdividing into the low and high temperature BB components.

Table 5
Results of Spearman Test and Power-law Fit to Parameter Correlations

Correlation[a]	PL Fit Index	Spearman Test	
		Correlation Coefficient	Chance Probability
	α		
$R_{\mathrm{high}}^2 \propto (R_{\mathrm{low}}^2)^{\alpha}$	3.1 ± 0.7	0.6	3.5×10^{-12}
$F_{\mathrm{high}} \propto F_{\mathrm{low}}^{\alpha}$	1.1 ± 0.1	1.0	0
$L_{\mathrm{high}} \propto L_{\mathrm{low}}^{\alpha}$	1.2 ± 0.1	0.9	5.6×10^{-45}
$R^2 \propto kT^{\alpha}$	-3.6 ± 0.2	-0.8	0
$R_{\mathrm{high}}^2 \propto kT_{\mathrm{high}}^{\alpha}$	-7.2 ± 1.3[b]	-0.7	7.4×10^{-13}
$R_{\mathrm{low}}^2 \propto kT_{\mathrm{low}}^{\alpha}$	0.3 ± 1.1[b]	-0.01	0.95
$E_{\mathrm{peak}} \propto F^{\alpha}$	0.09 ± 0.003[b]	0.6	8.2×10^{-6}
Γ versus F	⋯	0.4	1.5×10^{-3}

Notes.
[a] R^2, F, L, and kT are the emitting area, fluence, luminosity, and temperature of a BB, respectively.
[b] Power-law fit to the grouped data.

observed for the collection of SGR J1550−5418 bursts analyzed in the studies of Lin et al. (2012) and van der Horst et al. (2012). It is evident that for the entire BB+BB fitting ensemble, $R^2 T^4$ is an increasing function of T and hence also burst flux. Thus, brighter bursts are on average slightly harder in their BB+BB fits, noting that the same weak flux-hardness correlation is identified just below for the bursts with preferred COMPT fits.

The COMPT model fits 56 burst spectra well in our sample; seven bursts in the first episode and 48 in the second. Their parameter distributions and correlations are shown in Figure 4. We find the burst peak energy (E_{peak}) to range from 10 to 40 keV, with an average value of 26.4 ± 0.6 keV (derived with a Gaussian fit). The bottom left panel of Figure 4 shows the correlation of E_{peak} with fluence; here we display a weighted average of every 10 data points starting from the lowest fluence value due to the large scattering of the data. We clearly observe a positive correlation, indicating that the spectrum becomes harder as the burst fluence increases. The photon index (Γ) of the COMPT model also follows a Gaussian distribution, with a mean of -0.06 ± 0.12, over a range of -1.5 to -1.0. The bottom right panel of Figure 4 shows a weak correlation between Γ with burst fluence. We list the quantitative details of these correlations in Table 5.

4. Discussion

After about three years of quiescence, SGR J1935+2154 has entered another state of heightened burst activity, making it the most prolific transient magnetar. Remarkably, the number of bursts from the 2019 and 2020 episodes in this study, outnumber the total number of all previous bursts since its discovery, without even including the bursts emitted during the burst forest interval. We discuss below several interesting and somewhat intriguing characteristics from the source's new burst active episodes.

We present in the left panel of Figure 5, the temporal evolution of the total burst fluence in all burst active episodes since the discovery of SGR J1935+2154, as well as that of the average burst fluence (fluence per burst); both clearly show positive trends. Lin et al. (2020a) reported that the average burst energies (for a distance of 9 kpc) in its 2014, 2015, 2016

May, and 2016 June activity episodes were 0.4×10^{39}, 1.7×10^{39}, 2.8×10^{39}, and 8.2×10^{39} erg, respectively. This trend was suggestive of a future higher burst activity; contrary to this expectation, the average burst energies of the 2019 and 2020 episodes, of 5.9×10^{39} and 6.3×10^{39} erg, respectively, indicate a flattening of the average burst energy curve. However, these values correspond only to the 148 bursts studied here—adding the contribution of the burst forest in the 2020 episode significantly increases its final value (see the left panel of Figure 5). We consider, therefore, the current values as lower limits of the source energetics. This also takes into account the bursts that were missed when GBM was occulted by the Earth or in the South Atlantic Anomaly.

The distribution of the cumulative energy fluence for all 148 bursts from SGR J1935+2154 is shown in the right panel of Figure 5. This distribution is optimally represented with a broken PL, with indices of 0.31 ± 0.01 and 0.72 ± 0.02 for the lower and higher fluences, respectively. The break in the fluence occurs at $(1.2 \pm 0.1) \times 10^{-7}$ erg cm^{-2}. A single PL model also fits fluences above $S = 1 \times 10^{-7}$ erg cm^{-2}, which has generally been used in previous studies as the threshold for the 100% detection rate (van der Horst et al. 2012; Collazzi et al. 2015). The distribution of bursts with fluences $\geqslant 1 \times 10^{-7}$ erg cm^{-2} is well fit with a PL, with an index of -0.77 ± 0.01. This is very consistent with the PL index of -0.78 for the cumulative burst fluence in previous active episodes from this source (Lin et al. 2020a). It is important to note that although the 2019 and 2020 bursts were more energetic on average, they follow the same trend with past activations, as shown in the right panel of Figure 5.

The spectroscopy of the bursts provides information on the physical environment, where their emission originated. In general, by setting $E_{\mathrm{peak}} \sim 3kT_{e,\mathrm{max}}$, one obtains an estimate of the maximum for the effective plasma temperature T_e in the inner magnetospheric emission region. The τ_{bb} values vastly exceed the typical dynamical times $R_{\mathrm{NS}}/c \sim 3 \times 10^{-5}$ s for a neutron star radius $R_{\mathrm{NS}} \sim 10^6$ cm, so that plasma is nominally trapped in closed magnetic field line regions that are somewhat remote from the magnetic poles. Subsurface crustal dislocation by the strong fields likely leads to the energy deposition in the magnetosphere (Thompson & Duncan 1995), heating the pair plasma. With such an injection from the surface, effective temperature gradients are likely to be established due to the adiabatic cooling of gas as it expands to high altitudes. The convolution of such gradients will present itself as somewhat similar to the apparently nonthermal spectra in the data, masquerading as BB+BB or COMPT forms. The energetics of bursts guarantees optically thick plasma with highly saturated, Comptonized spectra at each magnetospheric locale, as discussed in Lin et al. (2011) and Lin et al. (2012). Within the total (putatively quasi-equatorial) emission region, energy conservation for the plasma+radiation transport from one zone to another connected by magnetic flux tubes dictates that when approaching thermal equilibrium, though not fully realizing it, the Stefan–Boltzmann law $R^2 T_e^4 = \mathrm{constant}$ is approximately satisfied. This is the physical origin of the observed high/low temperature coupling in the BB+BB fits.

Yet the BB fitting protocol does not automatically imply an absolutely thermal emission region. One can estimate the average detected flux $\mathcal{F}$ for each burst in Episode 2 using the total accumulated fluence listed in Table 2 divided by the number of bursts (125), further divided by $kT_{\mathrm{high}} \sim 15$ keV and
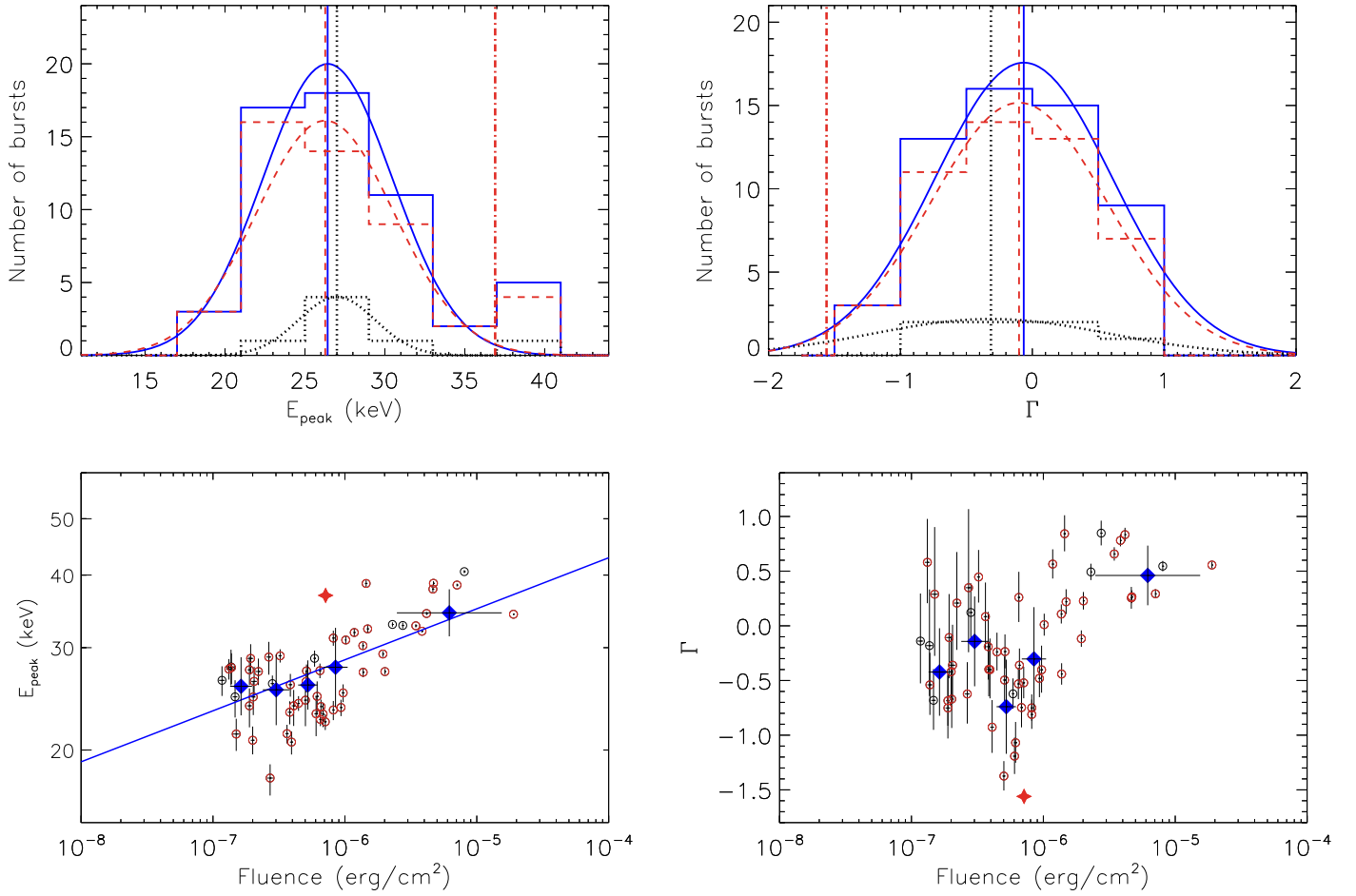
Figure 4. The top panels present distributions of $E_{\rm peak}$ (left) and Γ (right) of the COMPT model fits for all bursts (solid blue lines) and bursts in episodes 1 and 2 (dotted black and dashed red lines, respectively). The curves are Gaussian fits to the histograms; their mean values are represented by vertical lines. The lower panels show the $E_{\rm peak}$ (left) and Γ (right) as a function of fluence for all bursts. The bursts in episode 2 are highlighted with red circles. The filled blue diamonds represent the weighted means of consecutive groups of 10 data points each. The solid line is the best PL fit to the correlation between $E_{\rm peak}$ and fluence. The position of FRB 200428 is shown as a vertical dashed–dotted line in the top panels and as a red star in the bottom panels.
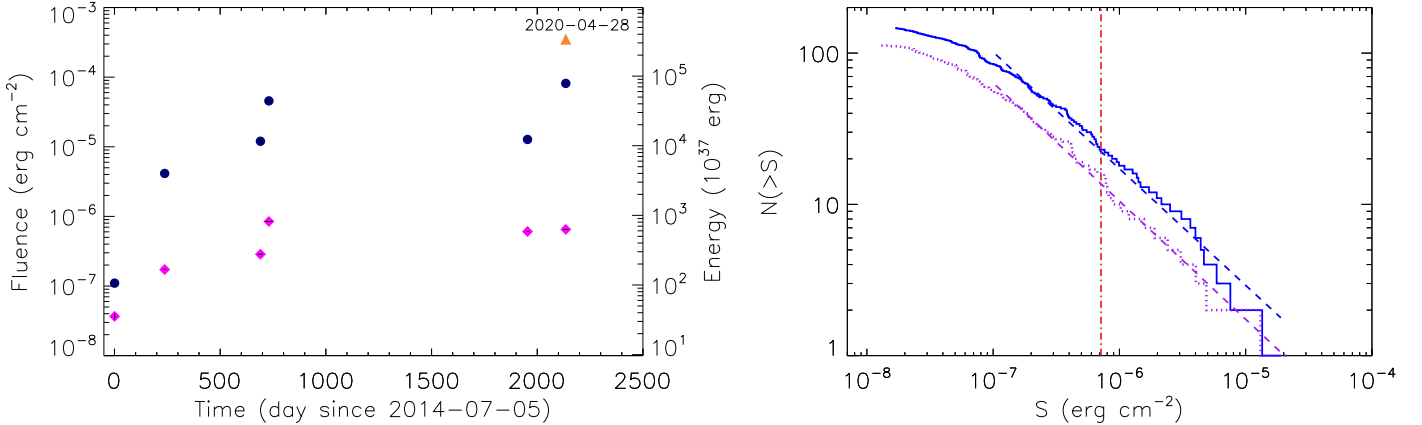
Figure 5. Left: time evolution of the total burst fluence (navy dots) and the average fluence per bursts (magenta diamonds from SGR J1935+2154 from discovery to present (left y-axis). The orange triangle is the total burst fluence including the burst forest on April 28. The corresponding burst energy, assuming a distance of 9 kpc, is shown in the right y-axis. Right: the cumulative energy fluence distributions of SGR J1935+2154 bursts in 2019–2020 (solid blue line) and 2014–2016 (dotted purple line). The two dashed lines are the best PL fit to the distribution above 1×10^{-7} erg cm^{-2}. The red vertical dashed–dotted line marks the fluence of the X-ray burst associated with FRB 200428.

also by the average $\tau_{\rm bb} \sim 200$ ms identified in Figure 2. From this, one can compute the photon number density $n_\gamma \sim \mathcal{F}d^2/(R^2 c)$ typically expected in the magnetospheric emission region. Assuming a source distance of $d = 9$ kpc and

an emission region size of $R = 10^6$ cm, one arrives at $n_\gamma \sim 3 \times 10^{24}$ cm^{-3}. This is considerably smaller than the density $0.24\,(kT_{\rm high}/[\lambda_{\rm C}\,m_e c^2])^3 \sim 10^{26}$ cm^{-3} of a pure Planck distribution of temperature $T_{\rm high}$, for a reduced electron
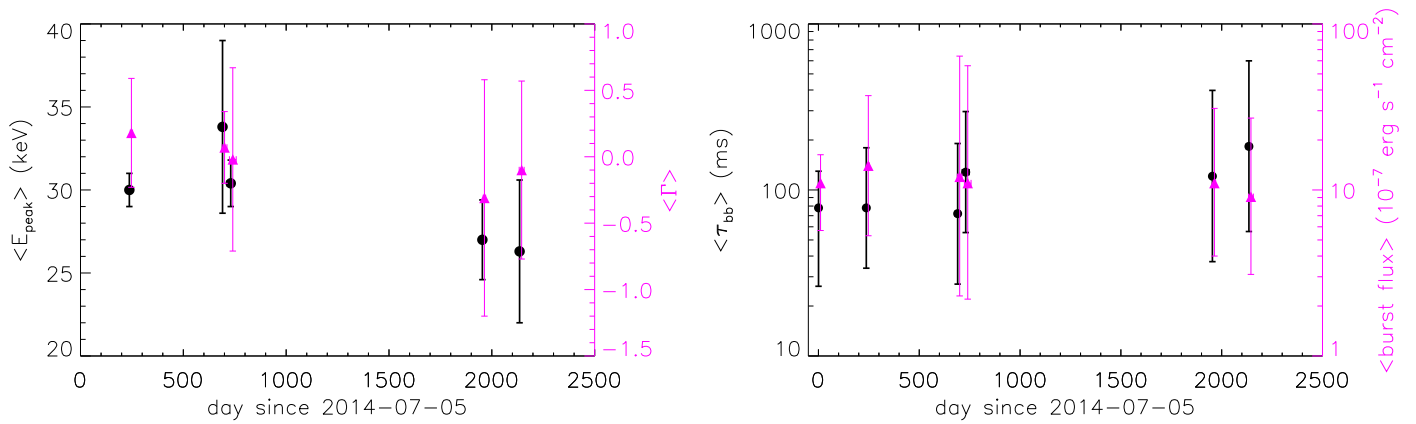
Figure 6. The evolution of E_{peak} (left, black dots), Γ (left, magenta triangles), τ_{bb} (right, black dots), and averaged burst flux (right, magenta triangles) in 8–200 keV throughout the six years of activity from SGR J1935+2154 (2014 to 2020). The error bars are the 1σ standard deviation of the Gaussian distribution. The magenta triangles are shifted to the right by 10 days for better visibility.

Compton wavelength $\lambda_C = \hbar/m_e c$. It is thus anticipated that thermalization is locally significant, though incomplete.

The comparison of the average[9] E_{peak} of bursts between 2014 and 2016 indicates a slight drop in hardness when progressing from that epoch to the 2019/2020 bursts in this study, although this variation is within the 1σ level: E_{peak} drops from ~30–35 keV to 27 keV, respectively (the left panel of Figure 6). Combining this trend with the rise in fluence exhibited in the left panel of Figure 5 over the same period suggests an anticorrelation between the average E_{peak} and fluence. Note that this is *opposite* to the E_{peak}–F trend in Figure 4 present for the 2019–2020 burst population. This evolutionary character is underpinned by an increase in the average burst duration τ_{bb} for the 2019–2020 bursts relative to the historic ones: see the right panel of Figure 6. We note that short bursts from other magnetars typically have an E_{peak} of ~40 keV (Collazzi et al. 2015), indicating that bursts from SGR J1935+2154 are also somewhat softer, corresponding to cooler plasma temperatures. Yet, noting the trend of increasing burst fluence over the 2014–2020 period, it is plausible to assume that the energy deposited into the magnetosphere (about 10^{39} erg) to precipitate these bursts is actually slightly increasing over this 6 yr interval. Given that the sizes of the emitting area for the high temperature BB component in our sample are consistent with that of other magnetars (van der Horst et al. 2012), we propose that the cooling of the maximum effective plasma temperature of SGR J1935+2154 bursts over time could correspond to greater masses and densities in the magnetospheric plasma emitting the bursts on average, and hence higher opacities. The likely coupling between such densities, temperature, and the spectral index as discussed in Lin et al. (2011, 2012) can help provide diagnostics for models of polarized radiative transport that lead to the generation of the spectra studied here.

A nonthermal spectrum has been reported for the hard X-ray burst associated with FRB 200428 from SGR J1935+2154 , with parameters $\Gamma \sim -1.5$ and $E_{peak} \sim 37$ keV when converted to our presentation here of the COMPT model (Li et al. 2020a). This peak energy is slightly higher than that of bursts with similar fluences in our sample[10] (see the lower left panel

of Figure 4). Therefore, the X-ray burst associated with the FRB is a slightly harder magnetar burst, yet with a noticeably steeper spectrum, a contrast highlighted in Younes et al. (2020a). As discussed above, this peculiar burst might have originated from a low density plasma region. Indeed the PL index of the burst associated with FRB 200428, as reported by Li et al. (2020a), is the steepest (softest) compared to the earlier bursts from SGR J1935+2154 or bursts from other magnetars. This is in agreement with the joint spectral analysis of GBM and NICER for SGR J1935+2154 (Younes et al. 2020a) and GBM and Swift/XRT data for SGR J1550−5418 (Lin et al. 2012). In order to reach a typical E_{peak} with a soft index, the overall spectral curvature needs to be rather flat, close to a power law with a relatively high cutoff energy (Li et al. 2020a; Ridnaia et al. 2020b). The 56 bursts in our sample that can be fit with the COMPT model reveal a softer E_{peak} with a typically harder photon index. This suggests a larger curvature in the spectral shape, indicating a more thermalized spectrum. This is also in agreement with the previous broadband spectral analysis of other magnetar bursts (Israel et al. 2008; Lin et al. 2012). A more thermalized spectrum may indicate an environment with a higher plasma density and thus scattering opacity, with the emission region perhaps spanning smaller ranges of magnetospheric altitudes. High opacity is extremely destructive for coherent radio emission mechanisms, and so it is reasonable to assert that radio signals are less likely to be generated in association with these putatively higher density bursts. This is in agreement with the nonradio detection of radio pulses from other SGR J1935+2154 bursts (Lin et al. 2020b).

Recently three faint FRB-like events from SGR J1935 +2154 were detected, one on 2020 April 30 (Zhang et al. 2020) and two on 2020 May 24 (Kirsten et al. 2020). At the time of the first radio burst, the GBM line of sight to the magnetar was occulted by the Earth. The times of the latter two events, which were separated by only 1.4 s from each other, were within the GBM field of view and their time span was covered by our search for untriggered events; we did not find any X-ray bursts coincident with these radio bursts. We place a 3σ flux upper limit in the 8–200 keV band of 2.2×10^{-8} erg cm^{-2} s^{-1}, assuming bursts with 0.5 s duration and with the same spectral shape with that of the burst associated with FRB 200428. This further implies that the flux ratio between X-ray and the 2020 May 24 radio events is less than 10^{-9} (erg cm^{-2})/(Jy ms).

---

[9] It is the mean value of the Gaussian fit to the distribution of E_{peak}. This is also the case for average Γ and τ_{bb}.

[10] The same result is reported independently using a subset of our sample (Yang et al. 2020).

ORCID iDs

Lin Lin ⬤ https://orcid.org/0000-0002-0633-5325
Ersin Göğüş ⬤ https://orcid.org/0000-0002-5274-6790
Oliver J. Roberts ⬤ https://orcid.org/0000-0002-7150-9061
Matthew G. Baring ⬤ https://orcid.org/0000-0003-4433-1365
Chryssa Kouveliotou ⬤ https://orcid.org/0000-0003-1443-593X
Yuki Kaneko ⬤ https://orcid.org/0000-0002-1861-5703
Alexander J. van der Horst ⬤ https://orcid.org/0000-0001-9149-6707
George Younes ⬤ https://orcid.org/0000-0002-7991-028X

References

Ambrosi, E., Barthelmy, S. D., D'Elia, V., et al. 2020, GCN, 27672, 1, https://gcn.gsfc.nasa.gov/gcn/gcn3/27672.gcn3
Barthelmy, S. D., Gropp, J. D., Kennea, J. A., et al. 2020, GCN, 27696, 1, https://gcn.gsfc.nasa.gov/gcn/gcn3/27696.gcn3
Bochenek, C. D., Ravi, V., Belov, K. V., et al. 2020, arXiv:2005.10828
Cash, W. 1979, ApJ, 228, 939
Cherry, M. L., Yoshida, A., Sakamoto, T., et al. 2020, GCN, 27623, 1, https://gcn.gsfc.nasa.gov/gcn/gcn3/27623.gcn3
Collazzi, A. C., Kouveliotou, C., van der Horst, A. J., et al. 2015, ApJS, 218, 11
Duncan, R. C., & Thompson, C. 1992, ApJL, 392, L9
Göğüş, E. 2014, AN, 335, 296
Göğüş, E., Kouveliotou, C., Woods, P. M., et al. 2001, ApJ, 558, 228
Gronwall, C., Gropp, J. D., Kennea, J. A., et al. 2020, GCN, 27746, 1, https://gcn.gsfc.nasa.gov/gcn/gcn3/27746.gcn3
Hurley, K., Cline, T., Mazets, E., et al. 1999, Natur, 397, 41
Hurley, K., Mitrofanov, I. G., Golovin, D., et al. 2020, GCN, 27625, 1, https://gcn.gsfc.nasa.gov/gcn/gcn3/27625.gcn3
Israel, G. L., Esposito, P., Rea, N., et al. 2016, MNRAS, 457, 3448
Israel, G. L., Romano, P., Mangano, V., et al. 2008, ApJ, 685, 1114
Kaspi, V. M., & Beloborodov, A. M. 2017, ARA&A, 55, 261
Kirsten, F., Snelders, M., Jenkins, M., et al. 2020, arXiv:2007.05101
Kouveliotou, C., Dieters, S., Strohmayer, T., et al. 1998, Natur, 393, 235
Kouveliotou, C., Meegan, C. A., Fishman, G. J., et al. 1993, ApJL, 413, L101
Li, C. K., Lin, L., Xiong, S. L., et al. 2020a, arXiv:2005.11071
Li, C. K., Tuo, Y. L., Ge, M. Y., et al. 2020b, GCN, 27679, 1, https://gcn.gsfc.nasa.gov/gcn/gcn3/27679.gcn3
Lin, L., Göğüş, E., Baring, M. G., et al. 2012, ApJ, 756, 54
Lin, L., Göğüş, E., Roberts, O. J., et al. 2020a, ApJ, 893, 156
Lin, L., Kouveliotou, C., Göğüş, E., et al. 2011, ApJL, 740, L16
Lin, L., Zhang, C. F., Wang, P., et al. 2020b, arXiv:2005.11479
Meegan, C., Lichti, G., Bhat, P. N., et al. 2009, ApJ, 702, 791
Mereghetti, S., Savchenko, V., Ferrigno, C., et al. 2020, ApJL, 898, L29
Olausen, S. A., & Kaspi, V. M. 2014, ApJS, 212, 6
Palmer, D. M. 2020, ATel, 13675, 1
Palmer, D. M., Barthelmy, S., Gehrels, N., et al. 2005, Natur, 434, 1107
Ridnaia, A., Golenetskii, S., Aptekar, R., et al. 2020a, GCN, 27631, 1, https://gcn.gsfc.nasa.gov/gcn/gcn3/27631.gcn3
Ridnaia, A., Svinkin, D., Frederiks, D., et al. 2020b, arXiv:2005.11178
Scargle, J. D., Norris, J. P., Jackson, B., & Chiang, J. 2013, ApJ, 764, 167
Stamatikos, M., Malesani, D., Page, K. L., & Sakamoto, T. 2014, GCN, 16520, 1, https://gcn.gsfc.nasa.gov/gcn/gcn3/16520.gcn3
The CHIME/FRB Collaboration, Andersen, B. C., Bandura, K. M., et al. 2020, arXiv:2005.10324
Thompson, C., & Duncan, R. C. 1995, MNRAS, 275, 255
van der Horst, A. J., Kouveliotou, C., Gorgone, N. M., et al. 2012, ApJ, 749, 122
von Kienlin, A., Gruber, D., Kouveliotou, C., et al. 2012, ApJ, 755, 150
Yang, Y.-H., Zhang, B.-B., Lin, L., et al. 2020, arXiv:2009.10342
Younes, G., Baring, M. G., Kouveliotou, C., et al. 2020a, arXiv:2006.11358
Younes, G., Guver, T., Enoto, T., et al. 2020b, ATel, 13678, 1
Younes, G., Kouveliotou, C., Jaodand, A., et al. 2017, ApJ, 847, 85
Zhang, C. F., Jiang, J. C., Men, Y. P., et al. 2020, ATel, 13699, 1